Parallel Assembly of Particles and Wires on Substrates by Dictating the Evolution of Instability in Liquid Metal Films

Jason D. Fowlkes[1,*], Lou Kondic[2], Javier A. Diez[3], Alejandro G. González[3], Yueying Wu[4], N. A. Roberts[4], Cliff E. McCold[5] and Philip D. Rack[1,4]

1. Center for Nanophase Materials Sciences, Oak Ridge National Laboratory, Oak Ridge, Tennessee, 37831–6493, *fowlkesjd@ornl.gov*

2. Department of Mathematical Sciences, Center for Applied Mathematics and Statistics, New Jersey Institute of Technology, Newark, New Jersey, 07102

3. Instituto de Física Arroyo Seco, Universidad Nacional del Centro de la Provincia de Buenos Aires Pinto 399, 7000, Tandil, Argentina

4. Materials Science and Engineering Department, The University of Tennessee, Knoxville, Tennessee, 37996–2200

5. Chemical Engineering & Materials Science, University of California, Davis, 95616

Supplement 1
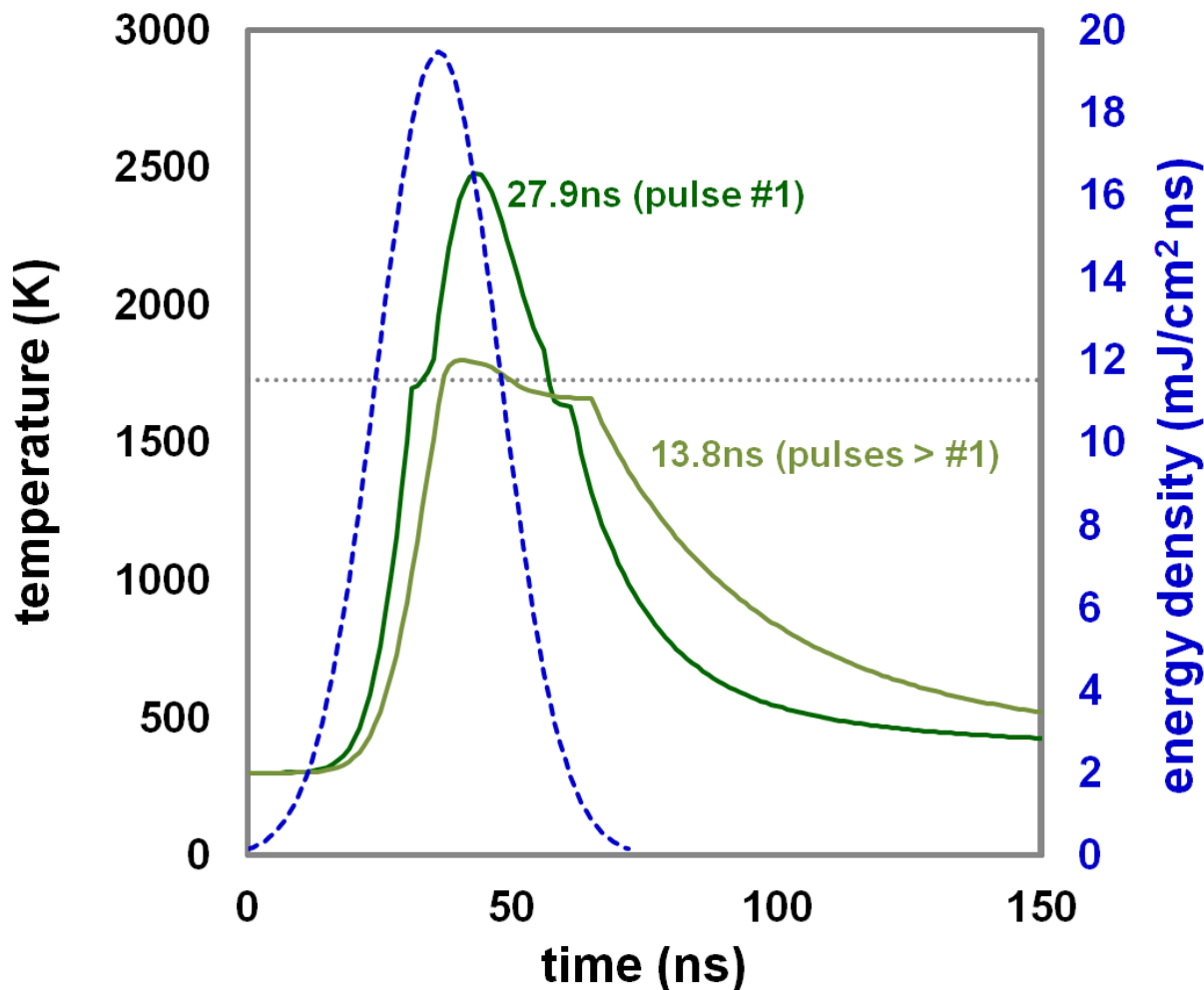
Figure S1 Finite element, time–temperature simulations for the case of the initial 10nm thick Ni film (27.9ns liquid lifetime) and the rivulet morphology (average thickness of 52nm, 13.8ns liquid lifetime). The temperature at the Ni/SiO$_2$ interface is shown. The Ni melting temperature is shown as the horizontal isotherm[1-4]. The Gaussian temporal beam pulse for a fluence of 220mJ/cm^2 with a beam pulse FWHM = 18ns is shown superimposed with the time–temperature profiles as the hatched, blue line[1]. The simulation considers the underlying 100nm SiO$_2$/Si substrate. The constant temperature boundary of T=300K was set at a position of z=25μm into the Si substrate. This boundary position was chosen because, beyond 25μm, negligible change was imposed on the time–temperature profile results at the metal–substrate interface.

Supplement 2

Metal evaporation decreased the total nanocap array volume relative to the initial thin film strip volume. The total mass evaporated during pulsed laser induced assembly was estimated by characterizing the final droplet contact angle, droplet width and droplet height (the key parameters required to characterize the cap morphology) using a combination of focused ion beam tracing and scanning electron microscopy (SEM). The density of the initial strip geometry and the final caps was assumed constant.

Focused ion beam tracing was used to mill a straight, narrow and shallow (~25nm) trench into the nanocap surfaces producing a trace for making subsequent measurements using SEM. The milling pattern was spatially oriented to pass through the position of maximum height of the spherical cap as well as parallel to the array of nanocaps as shown in figure S2a. The computer generated spherical cap replicas shown in figure S2a–c demonstrate the focused ion beam raster track used during focused ion beam tracing experiments. Milling time progresses from a) to c) in the illustration. SEM imaging in the orientation shown in figure S2e was required, following the focused ion beam tracing experiments, in order to characterize the cap geometric characteristics (figure S2d–e). The procedure is described further in the figure caption. The mass loss was also estimated for the case of the stable rivulet (figure S2f).
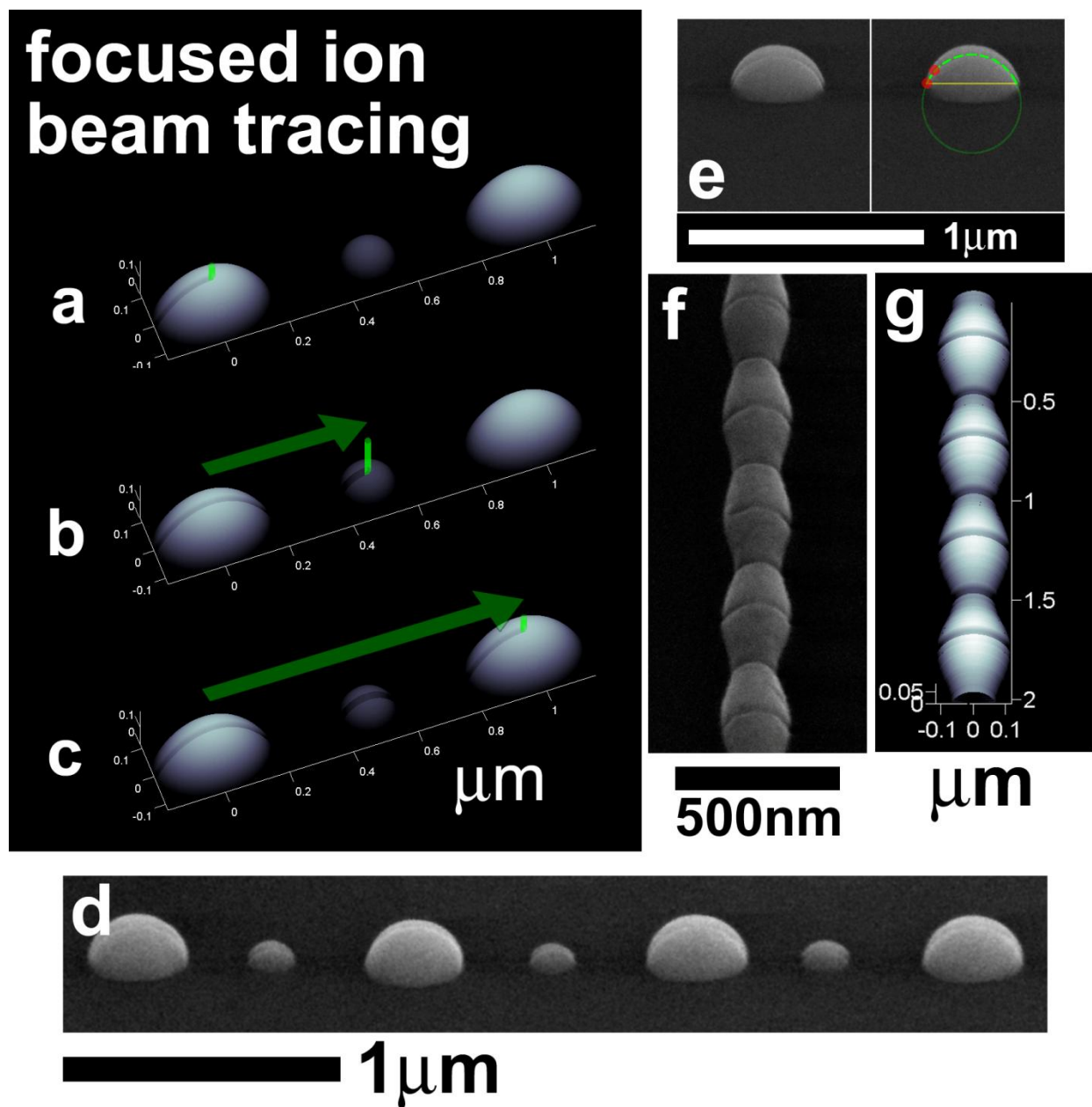
Figure S2 *a–c*) Time–lapse schematic of focused ion beam tracing across a computer generated replica of a nanocap array. The focused ion beam (green) traces a shallow and narrow trench across the nanocaps revealing characteristic geometric dimensions for subsequent scanning electron microscopy (SEM). *d*) An SEM image of an ion traced nanocap array taken at 52° with respect to the substrate normal and orthogonal to the ion trace. Primary caps as well as the smaller, satellite caps were included in the analysis *e*) a duplicate SEM showing the *left*) ion trace across the cap and *right*) an overlay of the critical dimensions that are extracted from the SEM image: contact width (yellow line), contact angle (red data points and yellow line) and height (blue line). This information made it possible to regenerate a replicate morphology (*a–c*) from which the

volume lost could be estimated relative to the initial mass in the thin film strip. An ellipsoidal cap morphology was used as the model morphology to reconstruct the primary caps while a spherical cap was used as the model for the satellite caps. *f)* Evaporation was also estimated for the case of the stable, rivulet morphology using the focused ion tracing method. This image was also taken at 52° with respect to the substrate surface normal. *g)* An example rivulet replica.
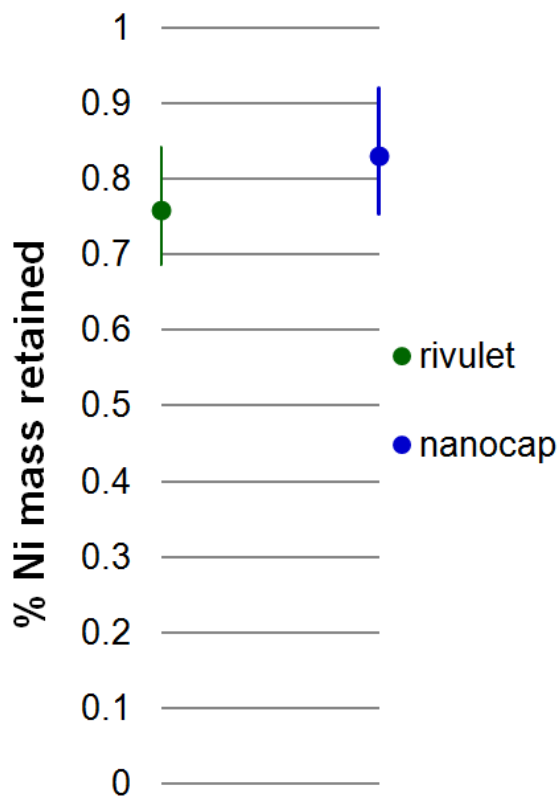
Figure S2_2 Estimated mass retained for stable rivulet and nanocaps array following 10 laser pulses at 220mJ/cm². The ±1nm height uncertainty for the initial thin film thickness was used to estimate the deviation.

Figure S2_2 shows the estimated mass retained for the Ni stable rivulet and nanocap array. The primary caps were best modeled using a truncated ellipsoid of the form;

$$\frac{x^2}{a^2} + \frac{y^2}{b^2} + \frac{z^2}{c^2} = 1, \ \ z > (c - h)$$

where a = 0.11, b = 0.24, c = 0.55 and h = 0.19µm. The satellite caps were modeled as spherical caps with a cap radius of 0.10µm and a wetting angle of 55°.

The rivulet morphology was modeled using the assumption of a truncated cylindrical cross–section. The contact width of the rivulet and the contact angle were obtained

from SEM images. With this information it was possible to construct a replicate rivulet. Specifically, for each column of pixels representing a transaxial slice of the rivulet, a circular cross–section was assumed and constructed. Such a replica is shown in figure S2g. Ion traces have also been included in the replica only to demonstrate the contact angle of the replica rivulet.

Supplement 3

An estimate of the temporal evolution of the rivulet half–width, in the substrate plane, was calculated using;

$$w_{1/2}(l,t) = \frac{w_o}{2} + A_o e^{\omega(\lambda)t} \cos \frac{2\pi l}{\lambda} \quad \textbf{1}$$

where $w_{1/2}(l,t)$ is the time–dependent half–width of the rivulet, w_o is the initial, mean rivulet width. We note that this is an approximation, since we are assuming that the linear stability analysis on which equation 1 is based is valid all the way until breakup. Estimates of unstable/stable mode breakup/decay were calculated at $l=0$. As a result, $cos(2\pi l/\lambda)=1$ and equation 1 simplifies to;

$$w_{1/2}(l,t) = \frac{w_o}{2} + A_o e^{\omega(\lambda)t} \quad \textbf{2}$$
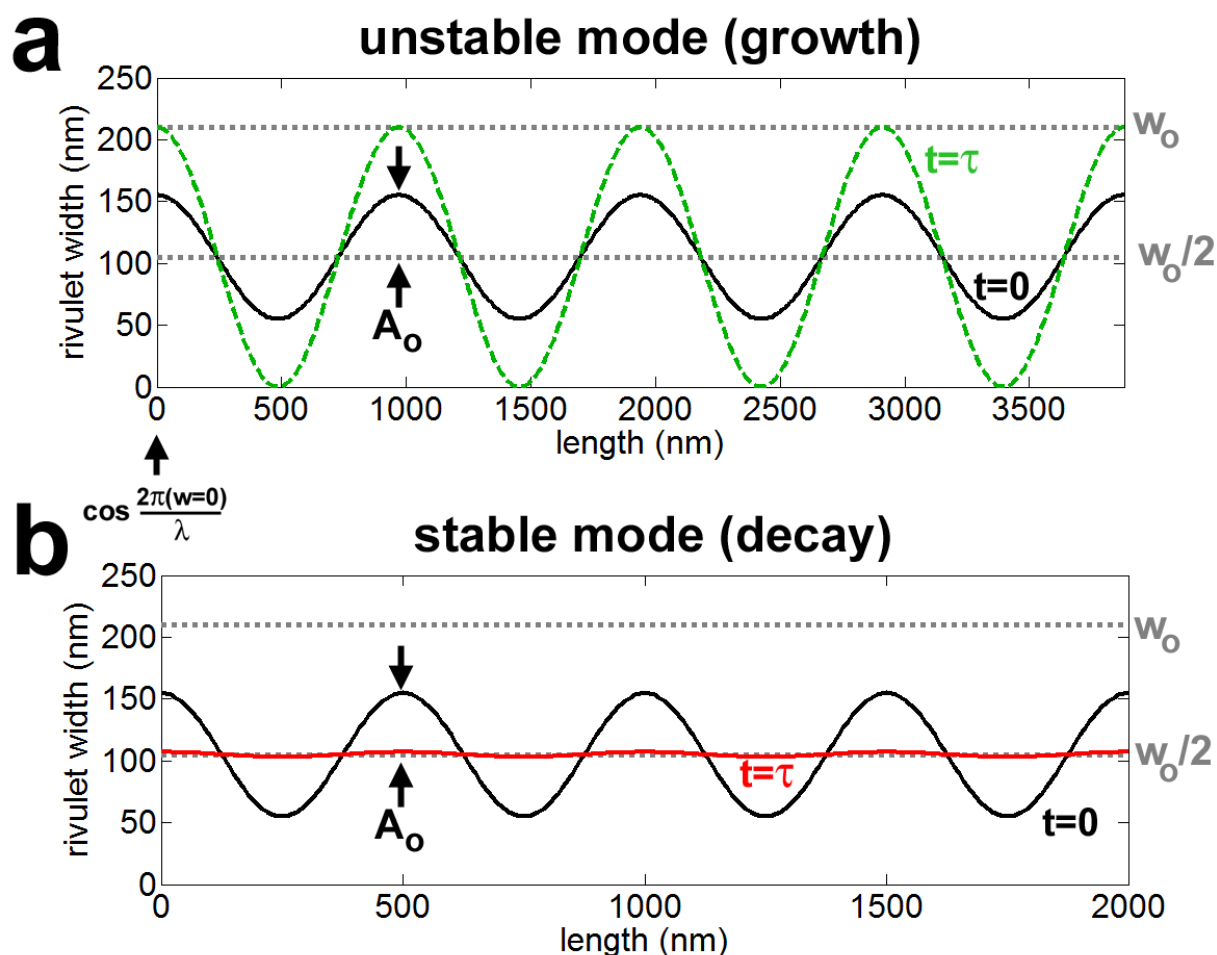
Figure S3_1 (a) An estimate of the rivulet half–width contact width with the substrate at the rivulet formation time (t=0) and at breakup (t=τ) for an unstable mode (λ=0.970μm, A_o=50nm). The half–width at break–up, $w_{1/2}(l=0,\tau)$, where pinching takes place in the

troughs, occurs when $w_{1/2}(l=0,\tau) = w_o$. (b) The case of stable mode decay (λ=500nm, A_o=50nm) where the completion of decay (t=τ) was taken as the average width of the rivulet plus an assumed nanoscale amplitude of 1nm.

Synthetic, unstable mode driven break–up

The rivulet break–up condition is characterized as;

$$w_{1/2}(l = 0, \tau) = w_o = 2R_o sin\theta \qquad \textbf{3}$$

for the unstable case where R_o is the radius of the rivulet, θ is the contact angle of the rivulet with the substrate, w_o is the contact width of the rivulet with the substrate and τ is the breakup time. Figure S3_1a shows the rivulet half–width for 4 periods of an unstable wavelength (λ=970nm) (black line) at the moment of rivulet formation. The initial amplitude of the synthetic perturbation on the rivulet edge is A_o=50nm for the example shown. The edge of the rivulet is shown at a later time (τ) as the hatched, green line plot. This breakup time, τ, is taken as the time when the trough of the rivulet "breaks", i.e., $w_{1/2}(l=\lambda/2,\tau)=0$, at ($l = \lambda/2$), or similarly, the peak reaches $w_{1/2}(l=0,\tau) = w_o$ at $l = 0$. An estimate of the break–up time was derived by inserting equation 3 into equation 2 and then rearranging.

$$\tau = \frac{1}{\omega(\lambda)} \ln \frac{R_o sin\theta}{A_o} \qquad \text{for } w_{1/2}(l=0) \quad \textbf{4}$$

Figure S3_2 shows the time evolution of the half–width for λ=0.970μm as a function of time. The green (w,l) plane shows the rivulet–substrate contact half–width at t=0 while the black (w,t) plane located at $cos(2\pi(l=0)/\lambda) = 1$ emphasizes the varicose peak amplitude as a function of time. The green line originally shown in figure 2 in the main text is reproduced in this plot along the top edge of the black, (w,t) plane.
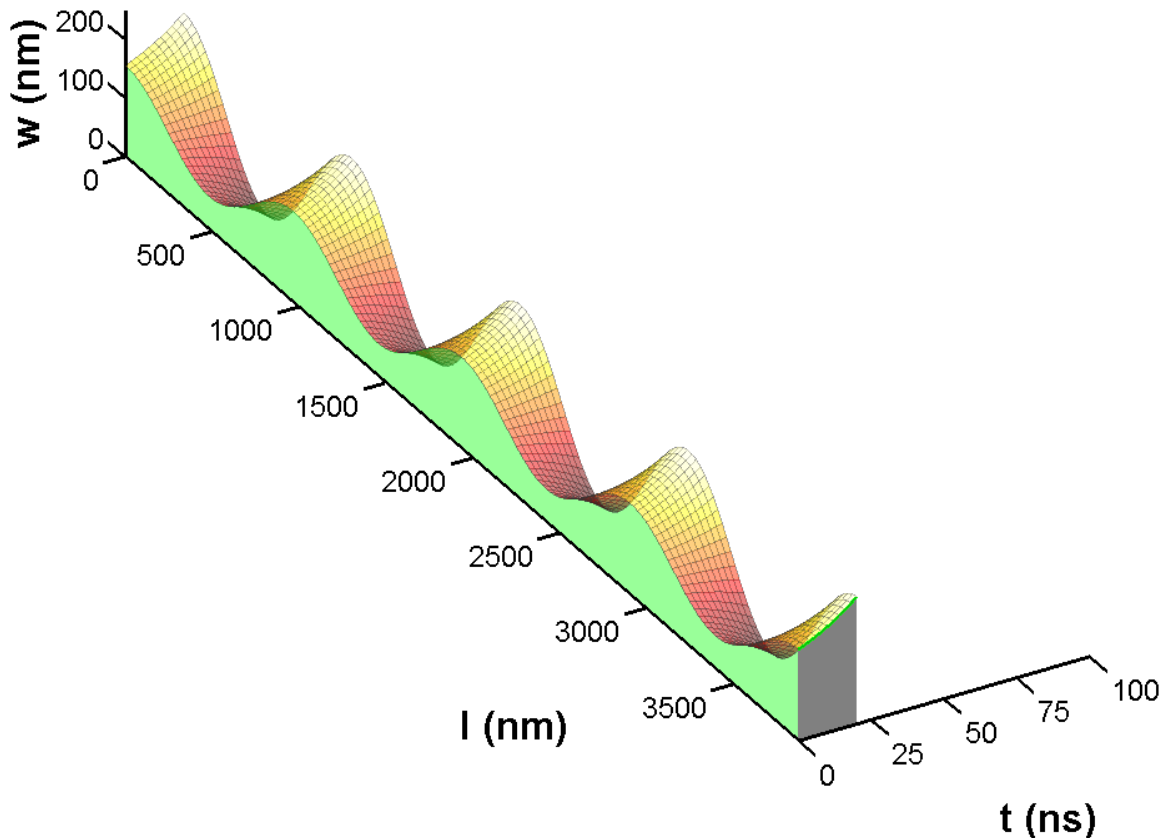
Figure S3_2 Visualization of unstable, synthetic rivulet development case up to the time of break–up estimated using equation 2 for $\lambda=0.970\mu m$, $A_o=50nm$ and $\Lambda=4$. Break–up is predicted at 18ns according to the growth rate of $\omega(0.970\mu m) = 0.040ns^{-1}$ derived using linear stability analysis.

Synthetic, stable mode driven decay

The stable mode decay condition is characterized as;

$$w_{1/2}(l = 0, \tau) = \frac{w_o}{2} + A_i \qquad\qquad \textbf{5}$$

for the stable case where A_i = 1nm and is the assumed value of the naturally evolving amplitude. Figure S3_1b shows the rivulet half–width for 4 periods (Λ) of a stable wavelength (λ = 500nm) (black line). The initial amplitude of the synthetic perturbation on the rivulet edge is $A_o=50nm$ for the example shown. The edge of the rivulet is shown at a later time (τ) as the hatched, red line plot. This (τ) is taken as the decay time where the varicose peak reaches the mean rivulet half–width plus the 1nm perturbation. An

estimate of the decay time was derived by inserting equation 5 into equation 2 and then rearranging.

$$\tau = \frac{1}{\omega(\lambda)} \ln \frac{A_i}{A_o} \quad \text{for } w_{1/2}(l=0,\tau) \qquad \textbf{6}$$

The lower limit of the breakup time for this rivulet is set by the superposition of the decay time (equation 6) plus the unstable, breakup time driven by the fastest growing mode. For our rivulet dimensions selected the fastest growing mode is $\lambda_m = 0.970\mu m$. The time to break–up, starting from the smoothened rivulet is governed by equation 4 where $A_o = A_i = 1nm$;

$$\tau = \frac{1}{\omega(\lambda)} \ln \frac{R_o \sin\theta}{A_i} \qquad \text{for } w_{1/2}(l=0,\tau) \qquad \textbf{7}$$

Figure S3_3 below shows the half–width evolution anticipated for a synthetic, stable mode showing both the stable mode decay plus the evolution of λ_m. In the experimental work presented in the main text, the number of pulses was not sufficient to produce breakup for the stable synthetic case. However, we have demonstrated this in a previous publication (Fig 4, ref 1)[1].
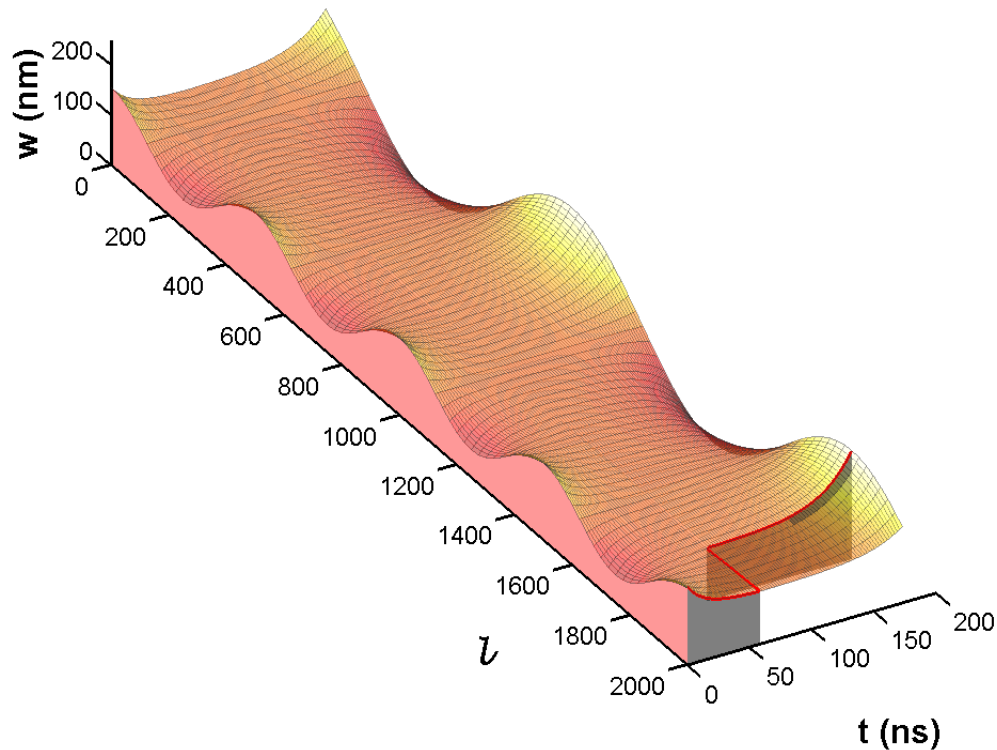
Figure S3_3   Visualization of the synthetic, stable rivulet evolution case up to the time of breakup estimated using equation 2 for $\lambda=0.500\mu m$, $A_o=50nm$ and $\Lambda=4$.   Decay is predicted to be complete at 61ns according to the decay rate of $\omega(0.500\mu m) = -0.068$ ns^{-1} derived from linear stability analysis. The fastest growing mode of $\lambda_m=0.970\mu m$, $A_o = A_i = 1nm$ was assumed to propagate following decay. Experiments have revealed that the unstable, fastest growing mode is uncorrelated in spatial phase with the original, stable synthetic mode; the stable mode decays followed by the spontaneous emergence of an unstable mode ($\lambda > \lambda_c$). Thus, a random phase was selected here for the spatial evolution of the unstable mode after 61ns. The fastest possible breakup is time is a linear combination of the decay time (61ns) plus the breakup time for $\lambda_m=0.970\mu m$ (116ns) which equals 177ns.

References

1.	J. D. Fowlkes, L. Kondic, J. Diez, Y. Y. Wu and P. D. Rack, *Nano Lett*, 2011, **11**, 2478-2485.
2.	P. D. Rack, Y. Guan, J. D. Fowlkes, A. V. Melechko and M. L. Simpson, *Appl Phys Lett*, 2008, **92**, 223108.
3.	Y. Wu, J. D. Fowlkes, P. D. Rack, J. A. Diez and L. Kondic, *Langmuir*, 2010, **26**, 11972-11979.
4.	Y. Wu, J. D. Fowlkes, N. A. Roberts, J. A. Diez, L. Kondic, A. G. Gonzalez and P. D. Rack, *Langmuir*, 2011, **27**, 13314-13323.